Made available through a Creative Commons CC-BY License

ACS APPLIED MATERIALS & INTERFACES

www.acsami.org Research Article

Noise Tailoring in Memristive Filaments

Botond Sánta, Zoltán Balogh, László Pósa, Dávid Krisztián, Tímea Nóra Török, Dániel Molnár, Csaba Sinkó, Roland Hauert, Miklós Csontos, and András Halbritter*

Cite This: *ACS Appl. Mater. Interfaces* 2021, 13, 7453−7460

Read Online

ACCESS | Metrics & More | Article Recommendations

ABSTRACT: In this study, the possibilities of noise tailoring in filamentary resistive switching memory devices are investigated. To this end, the resistance and frequency scaling of the low-frequency 1/*f*-type noise properties are studied in representative mainstream material systems. It is shown that the overall noise floor is tailorable by the proper material choice, as demonstrated by the order-of-magnitude smaller noise levels in Ta_2O_5 and Nb_2O_5 transition-metal oxide memristors compared to Ag-based devices. Furthermore, the variation of the resistance states allows orders-of-magnitude tuning of the relative noise level in all of these material systems. This behavior is analyzed in the framework of a point-contact noise model highlighting the possibility for the disorder-induced suppression of the noise contribution arising from remote fluctuators. These findings promote the design of multipurpose resistive switching units, which can simultaneously serve as analog-tunable memory elements and tunable noise sources in probabilistic computing machines.

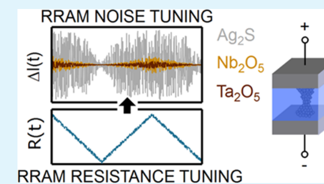

KEYWORDS: *resistive switching memory, memristor, niobium pentoxide, tantalum pentoxide, silver sulfide, noise, atomic fluctuation, two-level system*

■ INTRODUCTION

In traditional electrical engineering, noise is considered as an issue, which is to be suppressed to the lowest possible level.[1,2] Accordingly, the introduction of new components is usually preceded by lengthy material optimization steps to decrease the low-frequency, 1/*f*-type noise generated by material imperfections.[3,4] The emergence of novel neuromorphic computing architectures,[5,6] however, brings a paradigm change in noise engineering, demonstrating that tailored noise can be harvested as a useful computing resource in probabilistic computing schemes. As specific examples, stochastic magnetic tunnel junctions were utilized to solve integer factorization in a probabilistic bit computing architecture,[7] whereas a Hopfield neural network of resistive switching memory (RRAM) units was applied to solve nondeterministic polynomial-time (NP)-hard max-cut problems.[8] Noise tuning served as a key ingredient in the operation in both approaches.

Resistive switching memories, or memristors,[9,10] have already demonstrated their pioneering role in the development of information technologies, including energy-efficient, fast, and compact applications in mass data storage,[11] in-memory computing,[12] or the hardware implementation of artificial neural networks (ANNs).[13−16] In the latter case, the nonvolatile and analog-tunable RRAM resistance states serve as the neural weights of ANNs and dense crossbar RRAM architectures perform massively parallel operations, such as single time-step vector-matrix multiplication. Similar crossbar architectures served as the hardware accelerator in the above RRAM-based combinatorial optimization machines,[8] where the simulated annealing protocol was realized by the amplification/suppression of the intrinsic RRAM noise using an external hysteretic threshold circuitry.

To support further potential applications in noise engineering, here, we analyze how the intrinsic noise of RRAM devices can be tailored. More specifically, (i) we study the influence of material choice on the base noise level; (ii) we investigate how the relative noise level scales with the analog-tunable resistance states of RRAMs; and (iii) we deliver a fundamental understanding of the resistance scaling of the noise by model considerations. To this end, we analyze the resistance and frequency dependence of the intrinsic noise in Ta_2O_5- and Nb_2O_5-based resistive switching devices and compare these results to the markedly different noise levels observed in Ag-based resistive switching filaments. The above transition-metal oxide memristors represent well-established resistive switching systems with robust switching characteristics,[17,18] multilevel programming,[19,20] and ultrafast switching.[20,21] Ta_2O_5 is an especially widely studied compound with great potential for near-future neuromorphic computing applications.[6,22] Controversially, the noise analysis of these systems is very limited,[23−26] and the detailed investigation and understanding of the noise's resistance scaling is lacking. Our reference systems, the Ag-based filamentary devices, serve as another

Received: November 27, 2020
Accepted: January 25, 2021
Published: February 3, 2021

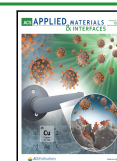

Downloaded via WIGNER RESEARCH CTR FOR PHYSICS on May 7, 2021 at 11:02:09 (UTC).
See https://pubs.acs.org/sharingguidelines for options on how to legitimately share published articles.

ACS Publications © 2021 The Authors. Published by American Chemical Society

https://dx.doi.org/10.1021/acsami.0c21156
ACS Appl. Mater. Interfaces 2021, 13, 7453−7460

fundamentally important platform in the RRAM technology.[27−33] Our related noise analysis[34] highlighted a universal resistance scaling behavior, revealing that the resistance fluctuations are dominated by the internal fluctuations of the Ag nanowires, whereas the embedding environment does not have an important influence on the noise.

The 1/f-type noise in nanoscale devices may originate from either atomic fluctuations or charge trapping/detrapping effects. In our previous study, we have demonstrated that our Nb_2O_5 scanning tunneling microscope (STM) point-contact devices preserve the metallic conduction through electronically transparent, unbroken filaments down to the level of single-atom diameters.[35] In this unbroken filamentary regime, charge-trap states in the embedding insulating matrix are efficiently screened by the metallic filament; therefore, we rather consider atomic fluctuations inside or at the surface of the filament as the dominant noise source. In the transition-metal oxide systems, we consider oxygen vacancies as the major fluctuators. In our further analysis, we solely treat this metallic unbroken filamentary regime, which is related to the resistance regime below the inverse conductance quantum, $G_0^{-1} \approx 12.9$ kΩ. This regime is favorable in RRAM crossbars utilized to implement vector-matrix multiplication operations.[6,14,15]

Previous noise studies have indicated that the noise level may depend of the resistance state in selected RRAM systems.[34,36−41] Prior studies mostly described the noise's resistance scaling in the metallic regime by a simple geometrical model relying on a cylinder (or prism) geometry with a single two-state fluctuator at the filament surface.[36,39−41] Here, we analyze the noise data in terms of our recently proposed model, which considers the scattering on dynamical defects (or two-level systems, TLSs) in a metallic point-contact geometry, also taking into account the crossover between the diffusive and ballistic transport regimes.[34] This model is able to describe an ensemble of fluctuators, which also accounts for the dominance of the fluctuators located nearby the narrowest part of the filament, and the suppressed contribution of more remote fluctuators. The fitting of the noise data with this model uncovers the material specificity of the two key parameters, the TLS density and the electron mean free path. Our analysis brings a counterintuitive conclusion demonstrating that the order-of-magnitude noise suppression of the transition-metal oxide resistive switching units compared to the Ag-based systems is primarily related to the enhanced level of disorder in the former material systems. This disorder enhancement yields an increased suppression of those "remote" fluctuators' noise contribution, which are located outside the narrowest region of the filaments.

■ RESULTS AND DISCUSSION

To study the noise characteristics of Ta_2O_5 and Nb_2O_5 memristive systems, we have applied two approaches: (i) we have established resistive switching junctions in both material systems by touching thin-film structures at various lateral positions with the PtIr tip of a custom-designed STM (see the insets in Figure 1a,b). With this approach, we could collect noise data on a statistical ensemble of independent junctions with various resistances. (ii) We have investigated the variation of the noise with the device resistance in $Al/Nb_2O_5/Pt$ crosspoint RRAM structures (see the inset in Figure 1c), where the resistance states were tuned by voltage pulses. The growth of the oxide layer was performed by either anodic oxidation (STM devices) or reactive sputtering (crosspoint devices). Both oxide growth protocols were optimized to achieve a pentoxide stoichiometry, which was confirmed by X-ray photoelectron spectroscopy (XPS) analysis. The peaks in the XPS spectra characteristic of the Ta_2O_5 and Nb_2O_5 compositions are demonstrated in Figure 1d,e, respectively. More details on the preparation and electroforming of the devices are provided in the Experimental Section. Figure 1a−c exemplifies the resistive switching current−voltage ($I(V)$) characteristics of the Ta_2O_5 (dark brown) and Nb_2O_5 (light brown) STM point-contact devices and Nb_2O_5 crosspoint devices (gray). We observed stable switching cycles, which are illustrated by the reproducibility of ≈100 consecutive $I(V)$ curves on each panel.

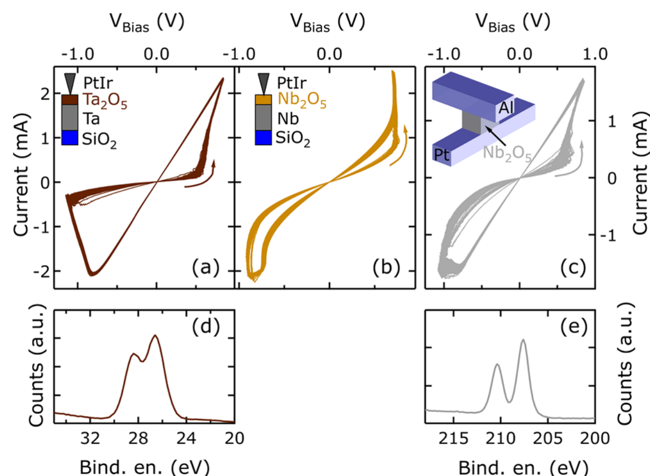

Figure 1. Representative resistive switching $I(V)$ curves of a $Ta/Ta_2O_5/PtIr$ (a) and $Nb/Nb_2O_5/PtIr$ (b) STM point-contact device and an $Al/Nb_2O_5/Pt$ crosspoint structure (c). The sample architectures are illustrated in the insets (see the Experimental Section for more details). It is noted that Nb_2O_5 resistive switching devices often exhibit highly nonlinear $I(V)$ characteristics (see panel (b)). This is attributed to the interplay of resistive switching in the core conducting filament and highly nonlinear Frenkel−Poole conduction[42,43] in the surrounding volume. This happens in devices where the switching threshold precisely coincides with the onset of the nonlinearity.[20,44,45] (d, e) XPS spectra measured on the surface of Ta_2O_5 layers established by anodic oxidation and Nb_2O_5 layers grown by reactive sputtering. The Ta_2O_5 composition was identified on the basis of the specific binding energies of 26.4 and 28.4 eV corresponding to the Ta^{5+} $4f_{7/2}$ and $4f_{5/2}$ states, whereas the binding energies of 210.4 and 207.7 eV identify the Nb^{5+} $3d_{3/2}$ and $3d_{5/2}$ states of Nb_2O_5. The C1s of the natural carbon surface contamination was shifted to 284.8 eV for charging compensation. A similar XPS spectrum of our Nb_2O_5 layers grown by anodic oxidation is available in ref 20.

A reliable noise study builds on the detailed understanding and careful separation of the simultaneous noise contributions present in the measurement setup and a corresponding data processing. Therefore, we first describe the scheme of our analysis shown in Figure 2. The measurement circuit (Figure 2c) includes a driving unit, the memristor device, a current amplifier, and an R_S serial resistor. The latter terminates the switching at the low-resistance state once the R_M memristor resistance becomes comparable to R_S. The V_{bias} voltage drop on the memristor junction is calculated as $V_{bias} = V_{drive} - I \times R_S$. More details on the measurement instrumentation are provided in the Experimental Section.

https://dx.doi.org/10.1021/acsami.0c21156
ACS Appl. Mater. Interfaces 2021, 13, 7453−7460

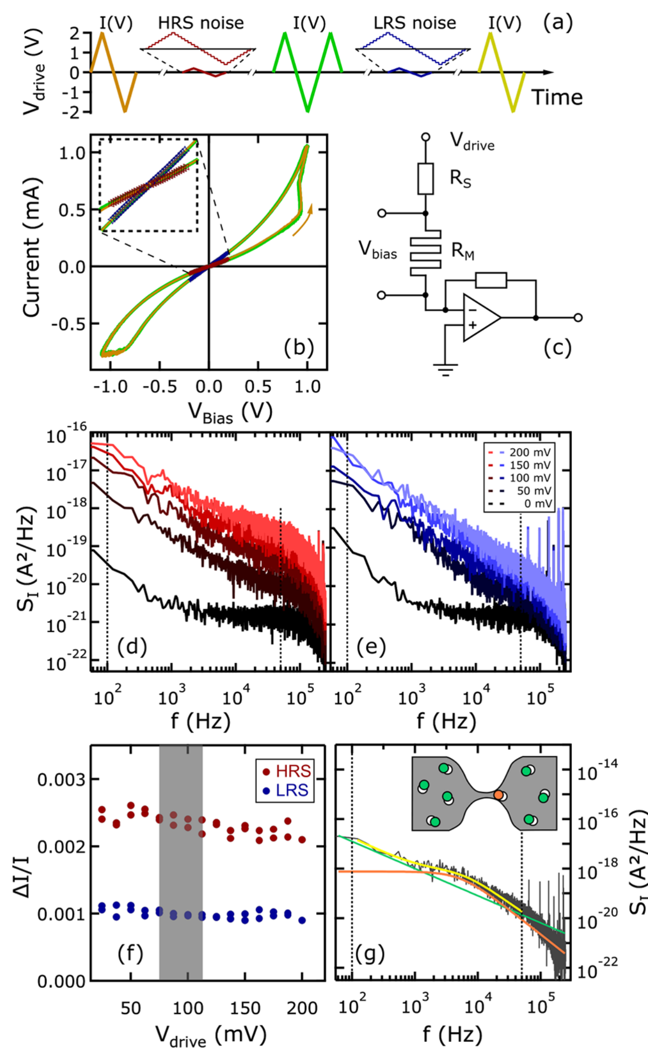

Figure 2. (a) Illustration of the sequence of higher driving voltage-level $I(V)$ measurements and intermediate-level noise measurements. (b) The first (brown) and second (green) resistive switching $I(V)$ curves of a $Nb/Nb_2O_5/PtIr$ STM point-contact junction together with the corresponding low-bias $I(V)$ branches evaluated from the noise measurement data acquired in the HRS (dark red) and LRS (dark blue). (c) Schematics of the measurement circuit (see text). (d, e) Bias voltage dependence of the current noise PSD measured along the HRS (red shades) and LRS (blue shades) $I(V)$ branches highlighted in (b). The black spectra correspond to the S_0 zero-bias background noise. The vertical dotted lines indicate the frequency interval, where the noise is integrated to calculate $\Delta I/I$. (f) Voltage dependence of $\Delta I/I$ as evaluated from data shown in (d) and (e). (g) Example noise spectrum of a memristive $Nb/Nb_2O_5/PtIr$ junction demonstrating the added contribution of a dominating fluctuator located close to the filamentary region (orange) and remote fluctuators (green) (see text).

Figure 2a illustrates the basic sequence of the measurement, which is illustrated by the $I(V)$ and noise data acquired in a particular Nb_2O_5 STM junction device (Figure 2b,d−f). First, a full-scale $I(V)$ curve is measured with a triangular V_{drive} signal exceeding the switching threshold, as exemplified by the light brown trace in Figure 2b. The voltage cycle leaves the junction in its high-resistance state (HRS). Next, a lower-amplitude voltage staircase is applied, where we evaluate the mean current (red curve in Figure 2b) and the power spectral density (PSD) of the current noise (Figure 2d) for each voltage step (see the Experimental Section for more details of the PSD calculation). Then, another higher-amplitude $I(V)$ measurement is performed (green curves in Figure 2a,b), preparing the junction in the low-resistance state (LRS) for the subsequent noise measurement (blue curves in Figure 2a,b,e). The sequence is completed by performing a final $I(V)$ measurement. To grant the mechanical stability of the STM point-contact devices, only those data are accepted for later analysis, where these three $I(V)$ curves are reproducible also agreeing with the low-bias $I(V)$ branches calculated from the voltage staircase data. In the case of the crosspoint devices, such a validation of each resistance state is not necessary. Instead, we measure the $I(V)$ curve at the beginning, and later positive and negative voltage pulses are used for the fine analog tuning of the resistance states. The noise is measured in each state with the same protocol using identical voltage staircase signals.

We wish to study the resistance scaling of the steady state $S_G(f) = (\Delta G)^2_f/\Delta f$ conductance noise PSD of the memristor junctions, where the $(\Delta G)^2$ mean-square conductance deviation is evaluated within a small Δf bandwidth around the central frequency f.[1] According to Ohm's law, this conductance noise PSD converts to current noise PSD as $S_I(f) = (\Delta I)_f^2/\Delta f = V^2 \times S_G(f)$, i.e., the V^2 voltage scaling of the current noise is a benchmark that the steady-state conductance noise is studied, and voltage-induced fluctuations and/or nonlinear features are excluded from the analysis. To evaluate the $\Delta I/I$ relative current fluctuation, we remove the S_0 zero-bias noise floor and integrate the current noise PSD in the frequency interval between 100 Hz and 50 kHz as $\Delta I/I = \sqrt{\int (S_I(f) - S_0(f))\mathrm{d}f/I^2}$. Note that in the case of steady-state noise measured in the linear part of the $I(V)$ curve, $\Delta I/I = \Delta G/G = \Delta R/R$ holds, and these relative current/conductance/resistance fluctuations are independent of the driving amplitude. Figure 2f demonstrates that the $\Delta I/I$ relative current fluctuations calculated from the spectra in Figure 2d,e are indeed voltage-independent within the scattering of the data, confirming that the steady-state conductance noise is measured in both states. For further analysis, we have set two criteria on the data: (i) the integrated noise PSD should be at least 1 order of magnitude larger than the S_0 noise floor integrated for the same band and (ii) nonlinear features should be excluded, i.e., we use a voltage interval, where the variance of the $R_M = V/I$ resistance and the $\Delta I/I$ relative current fluctuation are, respectively, less than 5 and 20% compared to the mean value for every device. Accordingly, we have used the 75−115 mV voltage interval for further analysis as a safe margin (see the gray interval in Figure 2f), where the negligibility of the background noise and nonlinear features is satisfied for all devices.

We have found that the frequency dependence of the noise spectra of Nb_2O_5- and Ta_2O_5-based memristors is often qualitatively different from the typical spectra acquired in Ag-based memristors.[34] In such cases, the $\log S_I$ vs $\log f$ spectrum cannot be fitted with a single line, rather a bump is superimposed on an $\sim 1/f^\gamma$ background, as exemplified in Figure 2g. This behavior can be modeled by a spatial distribution of the fluctuators, as illustrated in the inset of Figure 2g: a single (orange) fluctuator with a well-defined τ characteristic time is positioned very close to the narrowest part of the metallic filament, whereas the rest of the relevant fluctuators exhibiting various characteristic time scales (green) are more remote. In this case, the nearby fluctuator induces a

https://dx.doi.org/10.1021/acsami.0c21156
ACS Appl. Mater. Interfaces 2021, 13, 7453−7460

conductance noise with a temporal correlation function described by a single time constant, $C_G(\Delta t) = \langle \Delta G(t) \times \Delta G(t + \Delta t)\rangle = \langle \Delta G^2\rangle \times \exp(-\Delta t/\tau)$, yielding a Lorentzian noise spectrum in the frequency space: $S_G(f) = (4\langle \Delta G^2\rangle \times \tau)/(1 + (2\pi f)^2\tau^2)$ denoted by the orange line in Figure 2g. In the case of the remote fluctuators, the superposition of such Lorentzians characterized by different time constants yield a $1/f$-type envelope. The latter is well described by the $\sim 1/f^\gamma$ spectrum, where γ is usually close to unity, as represented by the green line in Figure 2g. Relying on this observation, we have evaluated all PSD spectra following two procedures: (i) we have calculated the numerical integral of the noise yielding the actual $(\Delta I/I)_{\mathrm{numint}}$ relative current fluctuation of the junction irrespective of the spectrum shape; (ii) we have fitted each spectrum with the superposition of a Lorentzian spectrum and a $1/f^\gamma$ spectrum (see the yellow fitting curve in Figure 2g). Based on the latter method, the relative current fluctuations arising from the nearby fluctuator, $(\Delta I/I)_{\mathrm{Lor}}$, and the remote fluctuators, $(\Delta I/I)_{1/f}$, can be decomposed by separately integrating the individual Lorentzian fitting function and the $\sim 1/f^\gamma$ term within the same 100 Hz to 50 kHz frequency band.

In Figure 3, we analyze the resistance scaling of the noise including its specificity to (i) the nature of the state (HRS or LRS), (ii) the preparation method (STM devices relying on anodic oxidation or crosspoint devices fabricated by reactive sputtering), and (iii) the material system (Nb_2O_5, Ta_2O_5, Ag_2S). Furthermore, we investigate the relative contribution of the nearby fluctuators as well as the γ frequency scaling exponent of the remote fluctuators. Finally, to extract the relevant parameters for practical noise engineering, we employ our recently proposed point-contact noise model.[34]

Figure 3a demonstrates the clear resistance scaling of $(\Delta I/I)_{\mathrm{numint}}$ evaluated in the HRSs (dark red) and LRSs (dark blue) of several Nb_2O_5 STM devices as well as of a Nb_2O_5 crosspoint device (gray). In the former case (STM devices), the data represent several (>20) independent point-contact junctions with various LRS and HRS resistances, whereas in the latter case, the multilevel programming of a particular crosspoint device was achieved by voltage pulses with typical amplitudes of $\pm(2-3)$ V (see the Experimental Section for the pulsing scheme). This analysis demonstrates that all of the blue, red, and gray data points follow the same resistance scaling tendency, implying that the noise is not specific to the preparation method, neither to the HRS or LRS nature of the state, but it solely depends on the device resistance in a certain material system. This conclusion agrees with our previous noise measurements on Ag-based filaments, where Ag_2S and AgI embedded as well as stand-alone Ag nanowires exhibited the same universal resistance scaling.

The black data points in Figure 3c–e show the resistance scaling of $(\Delta I/I)_{\mathrm{numint}}$ for Nb_2O_5, Ta_2O_5, and Ag_2S STM point-contact devices, respectively. To better resolve the average resistance dependencies, a statistical ensemble of noise data acquired on independent devices is grouped into resistance bins, which are equally spaced along the logarithmic resistance axis. The data points and error bars represent the mean values and standard deviations for the various noise measurements corresponding to a resistance bin. Note that the Ag_2S noise data represent our previous measurements acquired by a similar STM point-contact arrangement.[34] Here, these data are reevaluated according to the protocol used for the analysis of the Nb_2O_5 and Ta_2O_5 noise data in panels (c) and (d), i.e., we have evaluated $(\Delta I/I)_{\mathrm{numint}}$ in the same frequency band,

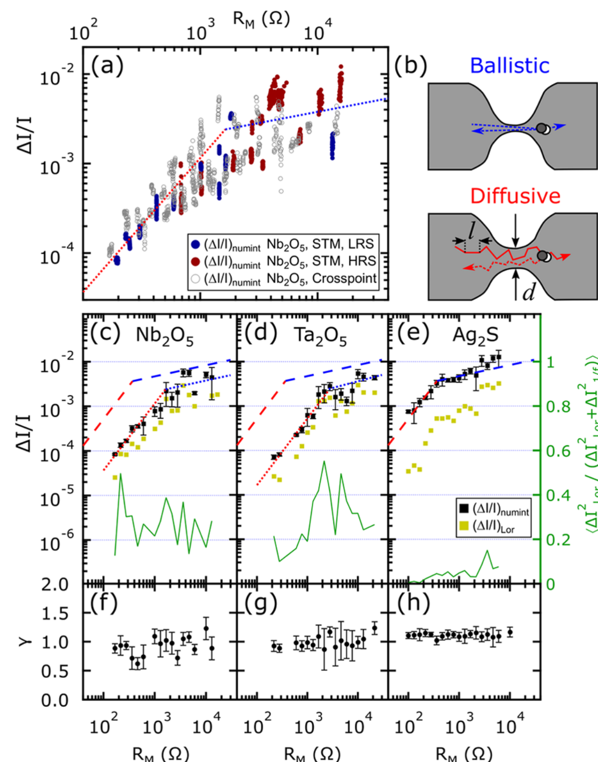

Figure 3. (a) Resistance scaling of $(\Delta I/I)_{\mathrm{numint}}$ for the HRSs (dark red) and LRSs (dark blue) of several independent Nb_2O_5 STM point-contact devices as well as for the voltage-tuned resistance states of a Nb_2O_5 crosspoint device (gray). As a reference, the model fitting function used in (c) is reprinted by the red/blue dotted lines. (b) Illustration of ballistic (diffusive) point-contact geometries. (c–e) The black (yellow) squares represent the resistance scaling of $(\Delta I/I)_{\mathrm{numint}}$ ($(\Delta I/I)_{\mathrm{Lor}}$). For each material system, the data rely on >20 independent junctions and 5 repeated $I(V)$ and noise measurement cycles on each junction, and from each noise measurement cycle, four different bias steps are used for the analysis (see the gray interval in Figure 2f). The best-fitting theoretical curves describe the diffusive (red) to ballistic (blue) crossover (see text). The fitting curves are calculated with the numerical values of $I_\Omega = 767.29$[34] and the $k_F = 1.2 \times 10^{10}$ m^{-1} coincident Fermi wavenumbers of Ag and Nb.[46] Relying on the similar band structures of Nb and Ta, we use the same value for Ta as well. The green curves and the corresponding green axis on the right show the relative noise contribution of the nearby fluctuator as deduced from the Lorentzian fitting component (see text). (f–h) Frequency scaling exponents as deduced from the $1/f^\gamma$ fitting component.

applied the resistance binning, and performed the decomposition of the $(\Delta I/I)_{\mathrm{Lor}}$ and $(\Delta I/I)_{1/f}$ contributions. This comparison shows that the noise increases with increasing resistance for all material systems; however, the overall noise level is markedly lower in the transition-metal oxide memristors than in the Ag_2S devices.

The $(\Delta I/I)_{\mathrm{Lor}}$ noise contribution of the nearby fluctuators is shown by the yellow dots in Figure 3c–e. This analysis also highlights a clear difference between the transition-metal oxide systems and Ag_2S: in the former case, the noise of the nearby fluctuators is comparable to the total noise, whereas in the latter, $(\Delta I/I)_{\mathrm{Lor}}$ is more than an order of magnitude smaller than $(\Delta I/I)_{\mathrm{numint}}$. This is also demonstrated by the green lines showing the relative noise contribution of the nearby fluctuators compared to the total noise, $(\Delta I_{\mathrm{Lor}})^2/((\Delta I_{\mathrm{Lor}})^2 + (\Delta I_{1/f})^2)$, demonstrating an ≈30% noise contribution of the

https://dx.doi.org/10.1021/acsami.0c21156
ACS Appl. Mater. Interfaces 2021, 13, 7453–7460

nearby fluctuators for Nb_2O_5 and Ta_2O_5, and a significantly smaller value for Ag_2S. We note that the statistically underpinned significance of nearby fluctuators in transition-metal oxide memristors agrees with previously reported $1/f^2$-type noise spectra of Ta_2O_5 RRAM devices[25] representing the high-frequency limit of a dominant Lorentzian spectrum.

The γ frequency scaling exponents are close to unity for all of the three systems, as shown in Figure 3f–h. Note that in the Ag_2S system, the noise spectrum is highly dominated by a $1/f$-type dependency, i.e., the fitting provides more precise values for γ. In contrast, the significant Lorentzian contribution in the Ta_2O_5 and Nb_2O_5 noise spectra also yields a consequently higher error in the fitted γ values.

In our previous work, we have quantitatively analyzed the resistance scaling of the noise in terms of our model taking electron scattering on dynamical defects (TLSs) into account.[34] In particular, the model considers the conducting filament as a point-contact device with a realistic geometry, where the ΔG conductance noise contribution of a dynamical defect scales with the probability that an electron returns to the junction after scattering on the TLS.[47] This return probability strongly depends on the relation of the d diameter of the junction and the l mean free path, i.e., the average distance at which the electrons loose their momentum due to scattering on lattice defects, impurities, or at the filament surface.[46] In the ballistic regime, where the l electron mean free path is larger than the d diameter (see Figure 3b (top), where the dark gray/white circles represent a TLS and the arrows illustrate possible electron trajectories), this return probability scales with the square of the solid angle at which the junction is seen from the TLS position. However, if d becomes larger than l (see Figure 3b (bottom)), the diffusive motion of the electrons reduces the return probability by a factor of $(2l/d)^2$ compared to the ballistic regime.[47] Relying on these geometrical coefficients and assuming a constant ρ_{TLS} TLS density as well as the validity of the Maxwell (Sharvin) conductance formulas in the diffusive (ballistic) regimes, we estimate the resistance scaling of the relative current fluctuations as[34]

$$\left(\frac{\Delta I}{I}\right)_{\text{diff}} = \frac{C\cdot k_F \times \sqrt{I_\Omega}}{\pi^{5/2} \times \sqrt{24}} \times (R_M G_0)^{3/2} \times \frac{l^{5/2}}{l_{TLS}^{3/2}} \quad (1)$$

$$\left(\frac{\Delta I}{I}\right)_{\text{ball}} = \frac{C \times \sqrt{I_\Omega}}{\pi^2 \times \sqrt{2k_F^3}} \times (R_M G_0)^{1/4} \times \frac{1}{l_{TLS}^{3/2}} \quad (2)$$

where $G_0 = 2e^2/h$ is the universal conductance quantum, k_F is the Fermi wavenumber, I_Ω is a constant resulting from a solid angle integral, $C = \Delta G/G_0$ sets the average amplitude of the conductance noise resulting from a TLS located at the center of the point contact, and $l_{TLS} = \rho_{TLS}^{-1/3}$ is the average spacing of neighbor TLSs. In the diffusive (ballistic) limit, $\Delta I/I$ scales with the 3/2 (1/4) power of the memristor resistance, respectively. Note that this model is derived for an orifice-like geometry, but it also well approximates a more realistic (e.g., hyperboloid) point-contact geometry.[47] This model has two fitting parameters, l and $C/l_{TLS}^{3/2}$. Using a $C = 0.5$ estimate,[34,48] we can extract the two relevant length scales, l and l_{TLS}, from the fitting. Note that the fitting is performed on the binned data in panels (c–e); however, the raw data (see the red and blue dots for the Nb_2O_5 STM point-contact junctions in panel (a)) and the binned data provide practically the same fitting results. This model fits well to our Ag_2S memristor noise data,[34] yielding $l_{Ag_2S} = 1.02 \pm 0.02$ nm and $l_{TLS,Ag_2S} = 1.93 \pm 0.03$ nm. The best-fitting curve composed of the diffusive and ballistic branches according to eqs 1 and 2 is shown by the red and blue dashed lines in Figure 3e. In Figure 3c,d, we fit the Nb_2O_5 and Ta_2O_5 noise data with the same model (red and blue dotted lines), yielding $l_{Nb_2O_5} = 0.484 \pm 0.036$ nm, $l_{TLS,Nb_2O_5} = 3.27 \pm 0.33$ nm, $l_{Ta_2O_5} = 0.380 \pm 0.021$ nm, and $l_{TLS,Ta_2O_5} = 3.71 \pm 0.29$ nm. As a reference, the fitting curve of the Ag_2S noise data is reproduced on both panels as a red/blue dashed line. The reduced noise level in the transition-metal oxide memristive systems compared to the Ag_2S data is the most pronounced in the diffusive regime, where Nb_2O_5 (Ta_2O_5) memristors exhibit a factor of ≈14 (≈31) reduction of $\Delta I/I$ with respect to Ag_2S devices, according to the offset of the diffusive fitting lines. This significant noise reduction has a twofold origin: the decrease of the electron mean free path and the decrease of the TLS density.

The above analysis allows us to draw clear conclusions on the aspects of noise engineering in the metallic regime of filamentary resistive switching memories:

(i) The diffusive regime is ideal for noise tailoring, as the $\Delta I/I \sim R_M^{3/2}$ resistance scaling is steep enough to customize the noise level within a sufficiently wide range by the analog tuning of the resistance states. As the ballistic regime is reached, a less steep resistance scaling is achieved, which hinders further noise tailoring. It is also noted that the mean free path is mainly extracted from the resistance threshold, where the noise evolution deviates from the diffusive scaling (≈1.5 kΩ, ≈2.5 kΩ, and ≈400 Ω for Nb_2O_5, Ta_2O_5, and Ag_2S, respectively). In the transition-metal oxide devices, this boundary is close to the inverse conductance quantum, $G_0^{-1} \approx 12.9$ kΩ, i.e., the ballistic regime spans less than an order of magnitude along the resistance axis. The even larger resistances are clearly outside the validity range of our point-contact model; however, other studies considering fluctuations in broken filaments reported saturated noise in the $R_M > G_0^{-1}$ regime.[36,38−41] Based on all of these, we propose the ≲2 kΩ (≲400 Ω) resistance range for the transition-metal-oxide (Ag_2S) systems as an optimal working range for noise tuning. At larger resistances (i.e., in the ballistic regime and in the regime of broken filaments), the saturated character of the relative noise levels is detrimental for efficient noise tailoring. Furthermore, in close vicinity to the inverse conductance quantum, the truly atomic-scale diameter of the filament introduces an extreme sensitivity to the precise atomic position of a nearby fluctuator.[25]

(ii) It is evident that the device noise can be reduced by decreasing the density of dynamical defects generating the noise, which was also demonstrated by a recent study relying on training-induced noise reduction.[49] Our analysis, however, highlights a further, less obvious noise reduction strategy via the suppression of the remote fluctuators' noise contribution by decreasing the electron mean free path. If the degree of static disorder can be increased without introducing further nearby fluctuators, the suppression of the remote fluctuators' noise delivers a significant overall noise reduction. Moreover, as the noise scales with a higher (5/2) power of l than l_{TLS} (3/2 power), a factor of 2 reduction in l yields twice as large reduction in $\Delta I/I$, as a factor of 2 increase in l_{TLS}

https://dx.doi.org/10.1021/acsami.0c21156
ACS Appl. Mater. Interfaces 2021, 13, 7453−7460

considering a constant memristor resistance. Alternatively, one can study the scaling of the relative current fluctuation as a function of the filament size by converting the memristor resistances to the d filament diameter according to the Maxwell (Sharvin) formula in the diffusive (ballistic) regime.[34] This conversion yields $(\Delta I/I)_{\mathrm{diff}} \sim l \times d^{-3/2} \times l_{\mathrm{TLS}}^{-3/2} \times k_F^{-2}$, and $(\Delta I/I)_{\mathrm{ball}} \sim d^{-1/2} \times l_{\mathrm{TLS}}^{-3/2} \times k_F^{-2}$, again demonstrating that the enhancement of static disorder yields noise reduction in the diffusive regime.

(iii) In the transition-metal oxide memristors, the noise contribution of remote fluctuators is so much suppressed that a single nearby fluctuator gives a major contribution to the total noise, which is a great advantage if noise reduction is targeted. However, the noise contribution of a single fluctuator is sensitive to the actual atomic position of the fluctuator within the narrowest filament region, which may change upon the resistive switching cycles. If noise tailoring is considered, it may be beneficial to eliminate this sensitivity by choosing material systems (like Ag-based memristors) with a higher overall noise level and a smaller relative contribution of the nearby fluctuators.

(iv) Finally, we consider the material aspects behind the significant noise suppression in transition-metal oxide filaments compared to Ag filaments. In the former case, the host metal is highly decorated with oxygen impurities. Furthermore, electron transport is dominated by d-orbitals, making the conductance sensitive to the details of the actual bond structure. Both aspects significantly decrease the mean free path of the electrons compared to Ag filaments, which are considered as pure metallic wires, where the highly delocalized *s* electrons are less sensitive to the actual atomic landscape. While the mean free path relies on all scattering processes including the static disorder of the filament, the noise solely originates from dynamical defects, where atoms are fluctuating between metastable positions. We consider unstable oxygen vacancies (Ag atoms) driven by temperature-activated Langevin dynamics[50] as the major noise sources in these transition-metal-oxide (silver) filaments. Interestingly, our analysis highlights that the enhanced level of static disorder in the Nb_2O_5 and Ta_2O_5 systems is not accompanied by an enhanced dynamical defect density. On the contrary, l_{TLS} is further increased compared to the Ag_2S system, i.e., these transition-metal oxide filaments are more stable against internal fluctuations than the Ag filaments.

CONCLUSIONS

In summary, we have performed a comparative study on the resistance scaling of the low-frequency noise in mainstream RRAM systems. We demonstrated that the noise characteristics of Ta_2O_5 and Nb_2O_5 memristors are well described by our point-contact model recently developed for the noise analysis of Ag-based filamentary resistive switches. In the diffusive transport regime, the relative noise levels of all of these systems exhibit a universal and sufficiently steep resistance scaling power for efficient noise tailoring. However, we found markedly different overall noise levels in the silver-based and the transition-metal-oxide-based systems. Our analysis yields a counterintuitive explanation for this difference highlighting the role of disorder-induced noise suppression in Ta_2O_5 and Nb_2O_5 memristors. This phenomenon is also reflected by the markedly different frequency scaling tendencies: in Ag-based filaments, the $1/f$-type spectrum is dominated by an ensemble of remote fluctuators, whereas in the Ta_2O_5- and Nb_2O_5-based systems, the frequency dependencies exhibit significant Lorentzian contributions due to the suppressed effect of remote TLSs and the dominance of single nearby fluctuators. These findings underpin the great potential of resistive switching memory technologies in novel probabilistic computing applications, demonstrating that besides the hardware implementation of analog-tunable neural weights, RRAM devices are also ideal candidates as tailorable noise sources. An optional application may follow the scheme in ref 51, where a memristor crossbar array accelerates the operation of a Hopfield neural network by performing the vector-matrix multiplications in single time-steps. An additional memristor row in the crossbar array is proposed as a tunable noise source. To find the global minimum in the energy landscape of the targeted computational problem, first, a larger noise can be applied, and then the noise is gradually decreased according to the simulated annealing protocol.

EXPERIMENTAL SECTION

Device Preparation. The Nb/Nb_2O_5 thin films were grown by Nb sputtering and subsequent anodic oxidation according to the protocol in ref 20, yielding ≈15 nm Nb_2O_5 on the top of a 300 nm thick Nb layer. The growth of the Ta/Ta_2O_5 thin films followed a similar procedure to ≈10/100 nm Ta_2O_5/Ta layer thickness. The oxide layer thickness values are extracted from XPS depth profiles. In the crosspoint devices, 0.8/50/16/60 nm layer thickness was adjusted for the (adhesive Ti)/$Pt/Nb_2O_5/Al$ layers using a 5 μm × 5 μm crosspoint cross section.

The $Al/Nb_2O_5/Pt$ crosspoint devices were fabricated according to the procedure in refs 18, 52, 53 adjusting the relative argon/oxygen content according to ref 52 to achieve Nb_2O_5 composition. In these devices, the Al layer reduces the Nb_2O_5 layer supplying mobile oxygen vacancies, which play a crucial role in the bipolar filamentary switching.[52]

Electroforming and Resistance Tuning. In the Nb_2O_5 crosspoint devices, the electroforming was performed by applying 500 μs long voltage pulses with gradually increasing amplitude on the memristor device and a 100 kΩ serial resistor. After each step, the pulse amplitude was increased by 1 mV. Between subsequent pulses, a lower-amplitude $I(V)$ curve was measured to read out the low-bias resistance. The forming process was stopped once the low-bias device resistance became smaller than 100 kΩ. This occurred typically after pulse amplitudes of 2−3 V. After the electroforming, the serial resistance was reduced to 1 kΩ or 100 Ω depending on the targeted LRS resistance, and the device was operated in the regime of unbroken metallic filaments. The multilevel programming was achieved by similar positive or negative writing pulses with somewhat smaller amplitudes (1−2 V) and similar readout $I(V)$ curves.

In the STM point-contact devices, mechanically sharpened PtIr tips were applied with a 250 μm wire diameter. A micron-scale tip-radius is estimated, with possible nanometer-scale protrusions. The forming is performed by the gentle mechanical approach of the thin film by the STM tip. This approach is stopped once the junction resistance becomes smaller than 100 kΩ. Afterward, a dedicated electroforming procedure is not required, and the junction is ready to study resistive switching $I(V)$ traces.[20] Note that the very similar noise characteristics of STM point contact and crosspoint Nb_2O_5 devices (see Figure 3a) imply that the fundamentally different forming steps of these two types of devices do not influence the noise characteristics.

Details of the Noise Measurement System. The measurement circuit (Figure 2c) supplies the V_{drive} driving voltage using an Agilent 33220A arbitrary waveform generator. An additional RC filter on the

https://dx.doi.org/10.1021/acsami.0c21156
ACS Appl. Mater. Interfaces 2021, 13, 7453−7460

output is utilized to further reduce the noise of the voltage source. The current through the memristor (I) is measured by a Femto DLPCA-200 current amplifier. The output of the amplifier is digitized with 22-bit resolution and 500 kS/s sampling rate with an NI PCI-5922 data acquisition card applying an antialiasing filter at the Nyquist frequency. At each constant voltage level, typically N = 100 000 data points are acquired. To avoid transient features, the first and last parts of this dataset are dropped and the remaining points are partitioned to nine segments with $N = 2^{13}$ points in each segment. For each segment, the noise spectrum is calculated by the fast Fourier transform (FFT) algorithm. Note that the spectral density of the current noise (or the noise PSD) is evaluated as

$$S_I(f) = \langle (2\Delta t/N) \times |\sum_{n=0}^{N-1} \Delta I(n\Delta t)\exp(-i2\pi fn\Delta t)|^2 \rangle \quad (3)$$

where Δt is the time delay between the neighbor acquisition events and $\Delta I(t)$ is the deviation of the current from its mean value. The noise spectra calculated for the nine segments are averaged.

AUTHOR INFORMATION

Corresponding Author

András Halbritter − *Department of Physics, Budapest University of Technology and Economics, 1111 Budapest, Hungary; MTA-BME Condensed Matter Research Group, 1111 Budapest, Hungary*; Email: halbritt@mail.bme.hu

Authors

Botond Sánta − *Department of Physics, Budapest University of Technology and Economics, 1111 Budapest, Hungary; MTA-BME Condensed Matter Research Group, 1111 Budapest, Hungary*

Zoltán Balogh − *Department of Physics, Budapest University of Technology and Economics, 1111 Budapest, Hungary; MTA-BME Condensed Matter Research Group, 1111 Budapest, Hungary*; orcid.org/0000-0002-9580-361X

László Pósa − *Department of Physics, Budapest University of Technology and Economics, 1111 Budapest, Hungary; Institute of Technical Physics and Materials Science, Centre for Energy Research, 1121 Budapest, Hungary*; orcid.org/0000-0001-7303-4031

Dávid Krisztián − *Department of Physics, Budapest University of Technology and Economics, 1111 Budapest, Hungary*

Tímea Nóra Török − *Department of Physics, Budapest University of Technology and Economics, 1111 Budapest, Hungary; MTA-BME Condensed Matter Research Group, 1111 Budapest, Hungary*; orcid.org/0000-0001-5238-5895

Dániel Molnár − *Department of Physics, Budapest University of Technology and Economics, 1111 Budapest, Hungary; MTA-BME Condensed Matter Research Group, 1111 Budapest, Hungary*

Csaba Sinkó − *Department of Physics, Budapest University of Technology and Economics, 1111 Budapest, Hungary*

Roland Hauert − *Laboratory for Joining Technologies & Corrosion, Empa, Swiss Federal Laboratories for Materials Science and Technology, CH-8600 Dübendorf, Switzerland*

Miklós Csontos − *Department of Physics, Budapest University of Technology and Economics, 1111 Budapest, Hungary; Transport at Nanoscale Interfaces Laboratory, Empa, Swiss Federal Laboratories for Materials Science and Technology, CH-8600 Dübendorf, Switzerland*; orcid.org/0000-0002-2766-6860

Complete contact information is available at: https://pubs.acs.org/10.1021/acsami.0c21156

Notes

The authors declare no competing financial interest.

ACKNOWLEDGMENTS

This research was supported by the Ministry of Innovation and Technology and the National Research, Development and Innovation Office within the Quantum Information National Laboratory of Hungary, and the NKFI K128534 grant. The support of the New National Excellence Program of the Ministry for Innovation and Technology is also acknowledged by B.S. (UNKP-19-3) and by T.N.T. and D.M. (UNKP-20-3).

REFERENCES

(1) Kogan, S. *Electronic Noise and Fluctuations in Solids*; Cambridge University Press, New York, 1996.
(2) Balandin, A. A. Low-Frequency 1/f Noise in Graphene Devices. *Nat. Nanotechnol.* **2013**, *8*, 549−555.
(3) Balandin, A. *Noise and Fluctuations Control in Electronic Devices*; American Scientific Publishers: Stevenson Ranch, Calif, 2002.
(4) Balandin, A.; Morozov, S.; Cai, S.; Li, R.; Wang, K.; Wijeratne, G.; Viswanathan, C. Low Flicker-Noise GaN/AlGaN Heterostructure Field-Effect Transistors for Microwave Communications. *IEEE Trans. Microwave Theory Tech.* **1999**, *47*, 1413−1417.
(5) Zidan, M. A.; Strachan, J. P.; Lu, W. D. The Future of Electronics Based on Memristive Systems. *Nat. Electron.* **2018**, *1*, 22−29.
(6) Xia, Q.; Yang, J. J. Memristive Crossbar Arrays for Brain-Inspired Computing. *Nat. Mater.* **2019**, *18*, 309−323.
(7) Borders, W. A.; Pervaiz, A. Z.; Fukami, S.; Camsari, K. Y.; Ohno, H.; Datta, S. Integer Factorization Using Stochastic Magnetic Tunnel Junctions. *Nature* **2019**, *573*, 390−393.
(8) Cai, F.; Kumar, S.; Vaerenbergh, T. V.; Sheng, X.; Liu, R.; Li, C.; Liu, Z.; Foltin, M.; Yu, S.; Xia, Q.; Yang, J. J.; Beausoleil, R.; Lu, W. D.; Strachan, J. P. Power-Efficient Combinatorial Optimization Using Intrinsic Noise in Memristor Hopfield Neural Networks. *Nat. Electron.* **2020**, *3*, 409−418.
(9) Chua, L. Memristor-The Missing Circuit Element. *IEEE Trans. Circuit Theory* **1971**, *18*, 507−519.
(10) Strukov, D. B.; Snider, G. S.; Stewart, D. R.; Williams, R. S. The Missing Memristor Found. *Nature* **2008**, *453*, 80−83.
(11) Yu, S.; Chen, P.-Y. Emerging Memory Technologies: Recent Trends and Prospects. *IEEE Solid-State Circuits Mag.* **2016**, *8*, 43−56.
(12) Li, C.; Belkin, D.; Li, Y.; Yan, P.; Hu, M.; Ge, N.; Jiang, H.; Montgomery, E.; Lin, P.; Wang, Z.; Strachan, J. P.; Barnell, M.; Wu, Q.; Williams, R. S.; Yang, J. J.; Xia, Q. In *In-Memory Computing with Memristor Arrays*, 2018 IEEE International Memory Workshop (IMW); IEEE, 2018.
(13) Alibart, F.; Zamanidoost, E.; Strukov, D. B. Pattern Classification by Memristive Crossbar Circuits Using Ex Situ and In Situ Training. *Nat. Commun.* **2013**, *4*, No. 2072.
(14) Li, C.; Hu, M.; Li, Y.; Jiang, H.; Ge, N.; Montgomery, E.; Zhang, J.; Song, W.; Dávila, N.; Graves, C. E.; Li, Z.; Strachan, J. P.; Lin, P.; Wang, Z.; Barnell, M.; Wu, Q.; Williams, R. S.; Yang, J. J.; Xia, Q. Analogue Signal and Image Processing with Large Memristor Crossbars. *Nat. Electron.* **2018**, *1*, 52−59.
(15) Li, C.; Belkin, D.; Li, Y.; Yan, P.; Hu, M.; Ge, N.; Jiang, H.; Montgomery, E.; Lin, P.; Wang, Z.; Song, W.; Strachan, J. P.; Barnell, M.; Wu, Q.; Williams, R. S.; Yang, J. J.; Xia, Q. Efficient and Self-Adaptive In-Situ Learning in Multilayer Memristor Neural Networks. *Nat. Commun.* **2018**, *9*, No. 2385.
(16) Boybat, I.; Gallo, M. L.; Nandakumar, S. R.; Moraitis, T.; Parnell, T.; Tuma, T.; Rajendran, B.; Leblebici, Y.; Sebastian, A.; Eleftheriou, E. Neuromorphic Computing with Multi-Memristive Synapses. *Nat. Commun.* **2018**, *9*, No. 2514.
(17) Lee, M.-J.; Lee, C. B.; Lee, D.; Lee, S. R.; Chang, M.; Hur, J. H.; Kim, Y.-B.; Kim, C.-J.; Seo, D. H.; Seo, S.; Chung, U.-I.; Yoo, I.-K.; Kim, K. A Fast, High-Endurance and Scalable Non-Volatile Memory

Device Made from Asymmetric Ta2O5-x/TaO2-x Bilayer Structures. *Nat. Mater.* **2011**, *10*, 625−630.
(18) Mähne, H.; Wylezich, H.; Hanzig, F.; Slesazeck, S.; Rafaja, D.; Mikolajick, T. Analog Resistive Switching Behavior of Al/Nb2O5/Al Device. *Semicond. Sci. Technol.* **2014**, *29*, 104002.
(19) Graves, C. E.; Dávila, N.; Merced-Grafals, E. J.; Lam, S.-T.; Strachan, J. P.; Williams, R. S. Temperature and Field-Dependent Transport Measurements in Continuously Tunable Tantalum Oxide Memristors Expose the Dominant State Variable. *Appl. Phys. Lett.* **2017**, *110*, 123501.
(20) Molnár, D.; Török, T. N.; Sánta, B.; Gubicza, A.; Magyarkuti, A.; Hauert, R.; Kiss, G.; Halbritter, A.; Csontos, M. In Situ Impedance Matching in Nb/Nb2O5/PtIr Memristive Nanojunctions for Ultra-Fast Neuromorphic Operation. *Nanoscale* **2018**, *10*, 19290−19296.
(21) Torrezan, A. C.; Strachan, J. P.; Medeiros-Ribeiro, G.; Williams, R. S. Sub-Nanosecond Switching of a Tantalum Oxide Memristor. *Nanotechnology* **2011**, *22*, 485203.
(22) Jeong, Y.; Lee, J.; Moon, J.; Shin, J. H.; Lu, W. D. K-means Data Clustering with Memristor Networks. *Nano Lett.* **2018**, *18*, 4447−4453.
(23) Terai, M.; Sakotsubo, Y.; Saito, Y.; Kotsuji, S.; Hada, H. Memory-State Dependence of Random Telegraph Noise of Ta2O5/TiO2 Stack ReRAM. *IEEE Electron Device Lett.* **2010**, *31*, 1302−1304.
(24) Choi, S.; Yang, Y.; Lu, W. Random Telegraph Noise and Resistance Switching Analysis of Oxide Based Resistive Memory. *Nanoscale* **2014**, *6*, 400−404.
(25) Yi, W.; Savelev, S. E.; Medeiros-Ribeiro, G.; Miao, F.; Zhang, M.-X.; Yang, J. J.; Bratkovsky, A. M.; Williams, R. S. Quantized Conductance Coincides with State Instability and Excess Noise in Tantalum Oxide Memristors. *Nat. Commun.* **2016**, *7*, No. 11142.
(26) Pan, Y.; Cai, Y.; Liu, Y.; Fang, Y.; Yu, M.; Tan, S.; Huang, R. Microscopic Origin of Read Current Noise in TaOx-Based Resistive Switching Memory by Ultra-Low Temperature Measurement. *Appl. Phys. Lett.* **2016**, *108*, 153504.
(27) Terabe, K.; Hasegawa, T.; Nakayama, T.; Aono, M. Quantized Conductance Atomic Switch. *Nature* **2005**, *433*, 47−50.
(28) Yang, Y.; Gao, P.; Gaba, S.; Chang, T.; Pan, X.; Lu, W. Observation of Conducting Filament Growth in Nanoscale Resistive Memories. *Nat. Commun.* **2012**, *3*, No. 732.
(29) Yang, J. J.; Strukov, D. B.; Stewart, D. R. Memristive Devices for Computing. *Nat. Nanotechnol.* **2013**, *8*, 13−24.
(30) Valov, I.; Sapezanskaia, I.; Nayak, A.; Tsuruoka, T.; Bredow, T.; Hasegawa, T.; Staikov, G.; Aono, M.; Waser, R. Atomically Controlled Electrochemical Nucleation at Superionic Solid Electrolyte Surfaces. *Nat. Mater.* **2012**, *11*, 530−535.
(31) Yang, Y.; Gao, P.; Li, L.; Pan, X.; Tappertzhofen, S.; Choi, S.; Waser, R.; Valov, I.; Lu, W. D. Electrochemical Dynamics of Nanoscale Metallic Inclusions in Dielectrics. *Nat. Commun.* **2014**, *5*, No. 4232.
(32) Wang, Z.; Joshi, S.; Savel'ev, S. E.; Jiang, H.; Midya, R.; Lin, P.; Hu, M.; Ge, N.; Strachan, J. P.; Li, Z.; Wu, Q.; Barnell, M.; Li, G.-L.; Xin, H. L.; Williams, R. S.; Xia, Q.; Yang, J. J. Memristors with Diffusive Dynamics as Synaptic Emulators for Neuromorphic Computing. *Nat. Mater.* **2017**, *16*, 101−108.
(33) Choi, S.; Tan, S. H.; Li, Z.; Kim, Y.; Choi, C.; Chen, P.-Y.; Yeon, H.; Yu, S.; Kim, J. SiGe Epitaxial Memory for Neuromorphic Computing with Reproducible High Performance Based on Engineered Dislocations. *Nat. Mater.* **2018**, *17*, 335−340.
(34) Sánta, B.; Balogh, Z.; Gubicza, A.; Pósa, L.; Krisztián, D.; Mihály, G.; Csontos, M.; Halbritter, A. Universal 1/f Type Current Noise of Ag Filaments in Redox-Based Memristive Nanojunctions. *Nanoscale* **2019**, *11*, 4719−4725.
(35) Török, T. N.; Csontos, M.; Makk, P.; Halbritter, A. Breaking the Quantum PIN Code of Atomic Synapses. *Nano Lett.* **2020**, *20*, 1192−1200.
(36) Ielmini, D.; Nardi, F.; Cagli, C. Resistance-Dependent Amplitude of Random Telegraph-Signal Noise in Resistive Switching Memories. *Appl. Phys. Lett.* **2010**, *96*, 053503.
(37) Soni, R.; Meuffels, P.; Petraru, A.; Weides, M.; Kügeler, C.; Waser, R.; Kohlstedt, H. Probing Cu Doped Ge0.3Se0.7 Based Resistance Switching Memory Devices with Random Telegraph Noise. *J. Appl. Phys.* **2010**, *107*, 024517.
(38) Fang, Z.; Yu, H. Y.; Fan, W. J.; Ghibaudo, G.; Buckley, J.; DeSalvo, B.; Li, X.; Wang, X. P.; Lo, G. Q.; Kwong, D. L. Current Conduction Model for Oxide-Based Resistive Random Access Memory Verified by Low-Frequency Noise Analysis. *IEEE Trans. Electron Devices* **2013**, *60*, 1272−1275.
(39) Ambrogio, S.; Balatti, S.; Cubeta, A.; Calderoni, A.; Ramaswamy, N.; Ielmini, D. Statistical Fluctuations in HfOx Resistive-Switching Memory: Part II—Random Telegraph Noise. *IEEE Trans. Electron Devices* **2014**, *61*, 2920−2927.
(40) Ambrogio, S.; Balatti, S.; McCaffrey, V.; Wang, D. C.; Ielmini, D. Noise-Induced Resistance Broadening in Resistive Switching Memory—Part I: Intrinsic Cell Behavior. *IEEE Trans. Electron Devices* **2015**, *62*, 3805−3811.
(41) Puglisi, F. M.; Zagni, N.; Larcher, L.; Pavan, P. Random Telegraph Noise in Resistive Random Access Memories: Compact Modeling and Advanced Circuit Design. *IEEE Trans. Electron Devices* **2018**, *65*, 2964−2972.
(42) Frenkel, J. On Pre-Breakdown Phenomena in Insulators and Electronic Semi-Conductors. *Phys. Rev.* **1938**, *54*, 647−648.
(43) Ielmini, D.; Zhang, Y. Analytical Model for Subthreshold Conduction and Threshold Switching in Chalcogenide-Based Memory Devices. *J. Appl. Phys.* **2007**, *102*, 054517.
(44) Slesazeck, S.; Mähne, H.; Wylezich, H.; Wachowiak, A.; Radhakrishnan, J.; Ascoli, A.; Tetzlaff, R.; Mikolajick, T. Physical Model of Threshold Switching in NbO2 Based Memristors. *RSC Adv.* **2015**, *5*, 102318−102322.
(45) Pickett, M. D.; Williams, R. S. Sub-100 fJ and Sub-Nanosecond Thermally Driven Threshold Switching in Niobium Oxide Crosspoint Nanodevices. *Nanotechnology* **2012**, *23*, 215202.
(46) Kittel, C. *Introduction to Solid State Physics*, 8th ed.; John Wiley & Sons, Inc, 2005.
(47) Halbritter, A.; Borda, L.; Zawadowski, A. Slow Two-Level Systems in Point Contacts. *Adv. Phys.* **2004**, *53*, 939−1010.
(48) Holweg, P. A. M.; Caro, J.; Verbruggen, A. H.; Radelaar, S. Ballistic Electron Transport and Two-Level Resistance Fluctuations in Noble-Metal Nanobridges. *Phys. Rev. B: Condens. Matter Mater. Phys.* **1992**, *45*, 9311−9319.
(49) Piros, E.; Lonsky, M.; Petzold, S.; Zintler, A.; Sharath, S.; Vogel, T.; Kaiser, N.; Eilhardt, R.; Molina-Luna, L.; Wenger, C.; Müller, J.; Alff, L. Role of Oxygen Defects in Conductive-Filament Formation in Y_2O_3-Based Analog RRAM Devices as Revealed by Fluctuation Spectroscopy. *Phys. Rev. Appl.* **2020**, *14*, 034029.
(50) Puczkarski, P.; Wu, Q.; Sadeghi, H.; Hou, S.; Karimi, A.; Sheng, Y.; Warner, J. H.; Lambert, C. J.; Briggs, G. A. D.; Mol, J. A. Low-Frequency Noise in Graphene Tunnel Junctions. *ACS Nano* **2018**, *12*, 9451−9460.
(51) Cai, F.; Kumar, S.; Vaerenbergh, T. V.; Liu, R.; Li, C.; Yu, S.; Xia, Q.; Yang, J. J.; Beausoleil, R.; Lu, W.; Strachan, J. P. *Harnessing Intrinsic Noise in Memristor Hopfield Neural Networks for Combinatorial Optimization* 2019, arXiv:1903.11194. arXiv.org e-Print archive. http://arxiv.org/abs/1903.11194.
(52) Mahne, H.; Wylezich, H.; Slesazeck, S.; Mikolajick, T.; Vesely, J.; Klemm, V.; Rafaja, D. In *Room Temperature Fabricated NbOx/Nb2O5 Memory Switching Device with Threshold Switching Effect*, 2013 5th IEEE International Memory Workshop; IEEE, 2013.
(53) Mikolajick, T.; Wylezich, H.; Maehne, H.; Slesazeck, S.; Mikolajick, T. In *Versatile Resistive Switching in Niobium Oxide*, 2016 IEEE International Symposium on Circuits and Systems (ISCAS); IEEE, 2016.

https://dx.doi.org/10.1021/acsami.0c21156
ACS Appl. Mater. Interfaces 2021, 13, 7453−7460